

Article

# Revisiting Enhanced AIS Detection Range under Anomalous Propagation Conditions

Irina Sirkova

Institute of Electronics, Bulgarian Academy of Sciences, 1784 Sofia, Bulgaria; irina@ie.bas.bg

**Abstract:** Two clear-air over-the-horizon propagation mechanisms affecting the Automatic Identification System (AIS) detection range are considered. Comparison results are presented between the path loss due to tropospheric ducting and path loss due to tropospheric scattering (troposcatter) for the AIS frequencies. The calculations are based on the well-known parabolic equation approximation to the wave equation, in which a simple troposcatter formula is incorporated. In most studied cases, the ducting ensures a significantly greater reduction in path loss than troposcatter even when the AIS frequencies are not well trapped in the duct. Emphasis is placed on the elevated trapping layers, and some features that may make ducting propagation less favorable in terms of increasing the AIS detection range are discussed.

**Keywords:** automatic identification system; anomalous propagation; tropospheric ducting; troposcatter; parabolic equation

## 1. Introduction

The automatic identification system, designed with the original goal of monitoring the navigation of ships in real time to avoid collisions, later included in the VHF data exchange system concept [1,2], has acquired, at present, much more importance in maritime communications than was originally supposed. A growing number of applications, such as weather forecasting and maritime traffic planning [3], use AIS data and rely on AIS performance [4]. At the same time, in a number of cases, it is enough to detect only part of the AIS message rather than decoding the entire message. The detection of only a fraction of the AIS messages sent by a vessel is sufficient for the purposes of locating and updating the vessel's position. In this sense, the detection range is the maximum distance from which the presence of a signal is detected (this does not mean that the information contained in the signal is read) [5]. According to [5], under normal propagation conditions and typical AIS parameters, the maximum reliable ship-to-ship communications distance is 37–46 km; the reliable distance for coast stations with higher antennas to receive AIS messages from ships reaches 64 km. Efforts are being made to increase both the communication and detection ranges up to 100 km and beyond [6]. The long range detection capability has lower reliability requirements than communication requirements; nevertheless, it cannot be achieved with the current AIS equipment specifications and line-of-sight (LoS) and diffraction propagation mechanisms [5]. Apart from equipment characteristics, AIS operation is affected by the weather and also by clear-air meteorological conditions. The latter determine the conditions for AIS signal propagation and thus contribute to increasing or decreasing the distance from which a signal is detected. This, with the lower reliability requirement for detection only rather than receiving the entire message, has drawn attention to the possible use of anomalous propagation mechanisms that provide transhorizon propagation of VHF radio waves and thus increase (eventually) the AIS detection range [5]. This work investigates by numerical simulations two clear-air anomalous propagation mechanisms associated with changes in tropospheric refraction, namely, the tropospheric ducting and the troposcatter, and compares their ability to increase the deep over-the-horizon propagation of AIS frequencies [7–12].



**Citation:** Sirkova, I. Revisiting Enhanced AIS Detection Range under Anomalous Propagation Conditions. *J. Mar. Sci. Eng.* **2023**, *11*, 1838. <https://doi.org/10.3390/jmse11091838>

Academic Editor: Fausto Pedro García Márquez

Received: 17 August 2023

Revised: 12 September 2023

Accepted: 19 September 2023

Published: 21 September 2023



**Copyright:** © 2023 by the author. Licensee MDPI, Basel, Switzerland. This article is an open access article distributed under the terms and conditions of the Creative Commons Attribution (CC BY) license (<https://creativecommons.org/licenses/by/4.0/>).

Over large bodies of water, the sharp gradients of water vapor and air temperature result in the deviation of tropospheric refraction from the standard one and can lead to the formation of tropospheric ducts. The vertical change in the refractive index of the air  $n$  is much larger than the horizontal change, and for practical purposes, the horizontal variations of  $n$  are often neglected. The introduction of the modified refractivity  $M$  defined as  $M = N + (z/a_e) \times 10^6$ , where  $N$  is the tropospheric refractivity,  $N = (n - 1) \times 10^6$ ,  $z$  is the height above the Earth surface and  $a_e$  is the Earth's radius, allows to treat the Earth surface as flat; the negative vertical gradient of  $M$  indicates the appearance of tropospheric duct (the corresponding gradient of  $N$  is  $dN/dz \leq -157$ ) [13]. For various reasons, such as the lack of real profiles or to facilitate calculations, the average height profiles of the modified refractivity  $M(z)$  approximated with bi-linear or tri-linear profiles are often used, which preserve the basic parameters of the ducts, except for the evaporation duct, modeled by a log-linear curve [14]. In Figure 1 are sketched the  $M(z)$  profiles for the essential duct types, with their basic parameters, duct thickness  $z_d$  and M-deficit, indicated. In the tropospheric duct, the electromagnetic (EM) energy of certain frequencies is trapped and propagated over a long distance as in a waveguide. Recently, considerable efforts have been made in studying the propagation characteristics of tropospheric ducts and investigating the associated over-the-horizon maritime propagation for specific regions or seas [10,11,15–17]. The evaporation duct attracted the attention of the authors of those papers because it is nearly permanently present above large bodies of water at lower and even moderate latitudes [18]. Other works investigate the possibility of using the evaporation duct to maintain efficient coastal communications links and their reliability [19–22]. Since frequencies ranging from about 1 GHz to 20 GHz are most affected by tropospheric ducting, all of the above papers focus on the microwave frequency range, while the less affected VHF band is somewhat neglected. In recent years, the ducted AIS signal propagation has been used mainly to detect anomalous propagation over the sea and estimate duct parameters [8,23–25]. As shown in [8,25], the influence of the evaporation duct on the VHF range is rather negligible; this range is more affected by surface and surface-based ducts.

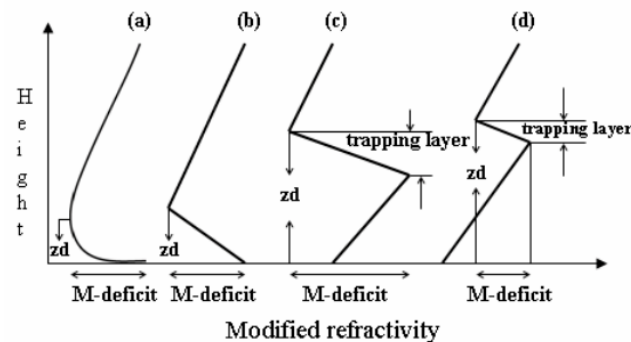


**Figure 1.**  $M(z)$  profiles for the essential duct types: (a) evaporation; (b) surface; (c) surface-based; (d) elevated.

Troposcatter is a mode of trans-horizon propagation of radio waves that results in random scattering from small-scale irregularities in the troposphere in the common volume encompassed by the transmitting and receiving antenna beams, see Figure 2. This propagation mechanism can extend coverage far beyond the diffraction zone and is applicable to a wide frequency range, including VHF [5]. The prediction of troposcatter loss is largely based on empirical models, as that proposed in [26,27], later developed in [28], and underlies the models in the recommendations of the International Telecommunication Union (ITU) [29]. At present, the recommendations in [29–31] are widely used to predict troposcatter losses. The recommendations in [30,31] are probability-based transmission loss prediction models: the first one is mainly used for interference prediction purposes for time percentages below 50%, while the second one is mainly used to predict propagation conditions for percentages greater than 50%. The recommendation in [30] provides climate zone

classification with application to troposcatter propagation and maps for their geographical application. A practical analysis and discussion on this model may be found in [12]. The troposcatter model [31] is a general purpose model that combines the two previous models. With the development of optimization methods, recently, more elaborated troposcatter models have been proposed, including one based on the genetic algorithm optimization of the problem parameters [32] and another based on particle swarm optimization in [33]. A review of recent studies on tropospheric scatter models may be found in [34].

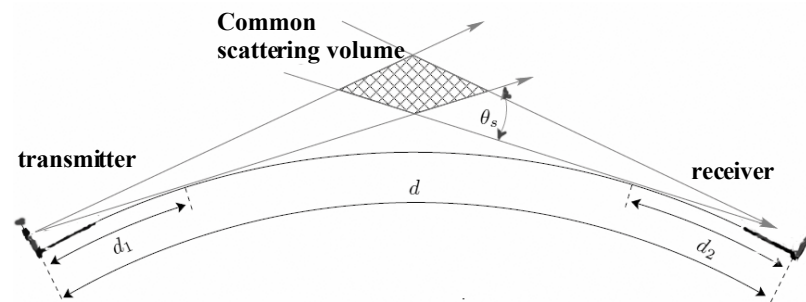


Figure 2. The geometry of the troposcatter model.

The complicated maritime conditions require sophisticated propagation models. To model the AIS frequency propagation under ducting, the parabolic equation (PE) approximation to the wave equation is used. This approximation allows the simultaneous use of non-linear refraction profiles and complex boundary conditions and also includes the antenna pattern [35–38]; at the same time, it can be efficiently solved numerically. A simple troposcatter formula [26,27] is incorporated in the PE model.

The paper is organized as follows: In Section 2, Section 2.1 provides a brief description of the PE method used for ducting propagation simulations and Section 2.2 describes the troposcatter model. In Section 3, the results obtained by the two methods from Section 2 are reported and discussed, and Section 4 is the conclusion.

## 2. Theoretical Background

### 2.1. Description of the PE Method

The PE-based numerical solution to various radio wave propagation problems is very well documented in the literature in different aspects: derivation [35,36] (a historical overview is provided in [39]), verification [40] and validation by comparisons with measured data [41–43]; at present, it is widely used to predict anomalous propagation in inhomogeneous environments, including coastal and maritime, and a broad range of frequencies [24,38,44]. In this work, the standard form of the 2D PE was applied, expressed by Equation (1):

$$\frac{\partial u(x, z)}{\partial x} = \frac{i}{2k_0} \frac{\partial^2 u(x, z)}{\partial z^2} + \frac{ik_0}{2} (m^2(x, z) - 1) u(x, z). \tag{1}$$

In Equation (1),  $k_0$  is the free-space wave number;  $m = M \times 10^{-6} + 1$  is the modified refractive index;  $u(x, z)$  is the reduced function [35], obtained from the transverse EM field component by removing the rapid fluctuating term  $\exp(ik_0x)$ ; and  $x$  and  $z$  are the horizontal and vertical coordinates, respectively. Equation (1) is solved numerically by marching algorithms, i.e., the solution at range  $x + \Delta x$  is obtained from that in the range  $x$ ; this requires knowledge of the EM field on an initial plane and the application of adequate boundary conditions. The numerical solutions of Equation (1) are based on finite difference (FD) algorithms, finite element (FE) algorithms or split-step Fourier-transform (SSF) algorithms. The choice of the numerical solution depends on the specifics of the propagation problem. Algorithms based on FD and FE are more flexible in modeling different boundary conditions and scattering surfaces, whereas SSF allows a larger horizontal

step size and is particularly suitable for propagation problems involving large distances. The main drawback of Equation (1) is that it does not account for backscattering. The applicability of the paraxial approximation and Equation (1) to the studied problem is ensured by the smooth variation of  $n$  with  $x$ , the grazing incidence angles involved in the ducted propagation and the fact that the EM field varies over scales much larger than the EM wavelength; under these conditions, the forward-propagated field has a dominant role. Equation (1) is very accurate for propagation angles within  $\pm 15^\circ$  of the preferred direction of propagation,  $x$  [35]; the studied problem falls within these limits. A larger discussion of the limitations of the 2D PE and its numerical solutions can be found in [38,45,46]. In this study, the SSF-based solution of (1) was used as described in [46] and implemented in “Advanced propagation model (APM) version 1.3.1 Computer software configuration item (CSCI) documents”, Tech. Doc. 3145. The PE model generates an output in terms of path loss ( $PL$ ,  $PL$  in dB) or propagation factor ( $PF$ ,  $PF$  in dB), calculated following Equation (2):

$$PL = 20 \log \left( \frac{4\pi d}{\lambda} \right) - PF, \quad PF = 20 \log |u(x, z)| + 10 \log(d) + 10 \log(\lambda), \quad (2)$$

where the first term in the  $PL$  expression is the free-space loss,  $\lambda$  is the free-space wavelength, and  $d$  is the transmitter–receiver distance. In this case, the definition of the  $PF$  corresponds to that provided in [13]:  $PF = |E/E_0|^2$ , where  $E$  is the electric field amplitude received at a given point under specific conditions and  $E_0$  is the electric field amplitude received in the same point under free-space conditions. This definition of the  $PF$  includes all propagation mechanisms between the two corresponding points accounted for by  $u(x, z)$ , including multipath and diffraction, as well as the transmitter antenna pattern.

In this study, the initial field was provided by an omni-directional antenna. A trans-horizon propagation path implies multiple reflections from the sea surface; therefore, the sea surface roughness should be accounted for. A good indicator of the surface roughness is the Rayleigh roughness parameter  $2k_0\sigma_h\sin(\alpha)$  [35], where  $\sigma_h$  is the standard deviation of the sea surface height and  $\alpha$  is the grazing incidence angle to the surface, i.e., the degree of roughness is determined not only by  $\sigma_h$  but also by the radio frequency and angle of incidence  $\alpha$ . The frequencies allocated to the AIS are centered at 161.975 MHz and 162.025 MHz and correspond to a wavelength of about 1.85 m. This is of the same order as  $\sigma_h$  obtained for high sea (sea state 7 from the Douglas sea scale) and applying one of the most widely used formulas that relates  $\sigma_h$  to the wind speed and sea state:  $\sigma_h = 0.0051 U_{10}^2$  [47], where  $U_{10}$  is the wind speed in m/s at  $h = 10$  m (for  $U_{10} = 15$  m/s  $\sigma_h = 1.15$  m). On the other hand, the ducting propagation implies small grazing angles, which reduce the influence of roughness. The significance of the sea surface roughness for AIS frequencies is still an open issue that is beyond the scope of this work. In this study, the sea surface roughness was neglected and the Fresnel reflection coefficient from a smooth surface was used. The dielectric characteristics of the sea water were taken from [28]. The environmental input to the PE was provided by  $M$  profiles calculated from meteorological data as in [48]; see Figures 3–5.

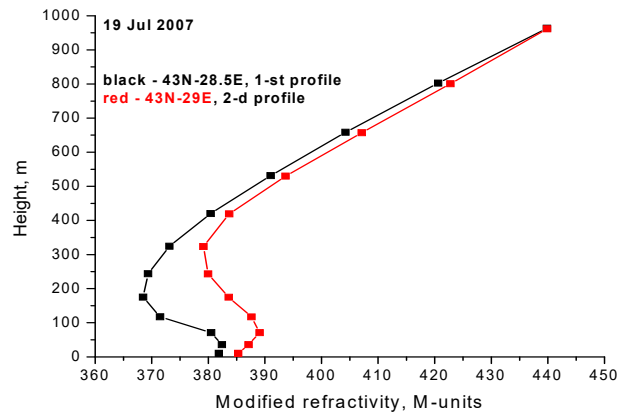


Figure 3. Surface-based duct profiles.

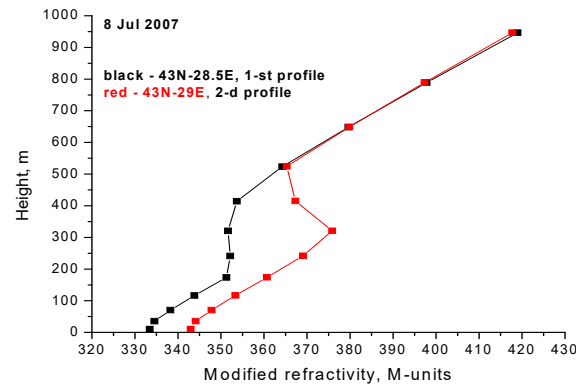


Figure 4. Elevated duct profiles.

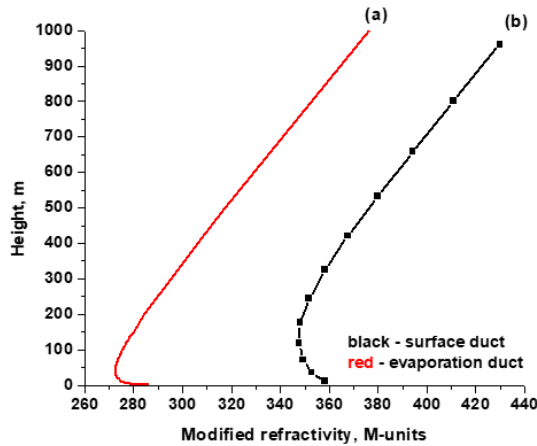


Figure 5. Evaporation duct profile (a); surface duct profile (b).

### 2.2. Troposcatter Model

At ranges deep beyond the radio horizon when there are no trapping layers and ducting, the scattering from irregularities in the troposphere in the common volume encompassed by the transmitting and receiving antenna beams becomes the dominant propagation mechanism. It applies for frequencies from around 100 MHz to above 8000 MHz. In this study, the troposcatter is considered in the category of anomalous propagation mechanisms. It should be noted, however, that the troposcatter is a more stable and predictable mechanism than the appearance of trapping layers and tropospheric ducts. Nevertheless, as pointed out in [5], the path losses due to troposcattering are relatively large and cannot

provide reliable ship-to-shore reception of AIS messages with the current AIS shore station design, but it still can be used for message detection. The troposcatter model used in this work follows that described in [26]. The median path loss in the troposcattering region, in dB, is expressed by:

$$PL = 115.4 + 10\theta_s + 20 \log(d) + 30 \log(f) - 0.2N_0, \tag{3}$$

where  $\theta_s$  denotes the scattering angle in degrees (see Figure 2),  $d$  is the ground transmitter-receiver distance in km,  $f$  is the frequency in MHz, and  $N_0$  ( $N$ -units) is the sea-level surface refractivity. Note that at sea level  $M(z = 0) = M_0 = N_0$ . Formula (3) is mainly experimentally obtained and comprises three components [26]: free space loss,  $L_{fs}$ , expressed by Formula (4); year-round median scatter loss for mean year surface refractivity  $N_0 = 310$   $N$ -units,  $L_s$ , expressed by Formula (5); and the term  $-0.2(N_0 - 310)$  that accounts for the geographical variations in troposcattering:

$$L_{fs} = 32.44 + 20 \log(d) + 20 \log(f), \tag{4}$$

$$L_s = 57 + 10(\theta_s - 1) + 10 \log\left(\frac{f}{400}\right), \text{ for } \theta_s > 1^\circ. \tag{5}$$

For smooth earth, the scattering angle is:

$$\theta_s = \frac{180}{\pi} \frac{d - (d_1 + d_2)}{ka_e}, \quad d_1 = \sqrt{2ka_e h_t}, \quad d_2 = \sqrt{2ka_e h_r}, \tag{6}$$

where  $h_t$  and  $h_r$  are the transmitter and receiver heights, respectively;  $a_e = 6370$  km is the Earth radius; and  $k$  is the effective earth radius factor. For a standard troposphere,  $k = 1.3333$ ; usually this value is used in troposcatter calculations.

It is difficult to strictly distinguish the range of application between the diffraction propagation mechanism, calculated by PE, and troposcatter mechanism where Equation (3) applies. In this case, we used the minimum range  $r_d$  at which the diffraction solution is applicable as a criterion [49]:

$$r_d = r_{hor} + 230.2 \left(\frac{k^2}{f}\right)^{1/3}, \quad r_{hor} = 3.572 \left(\sqrt{kh_t} + \sqrt{kh_r}\right), \tag{7}$$

where  $r_{hor}$  is the radio horizon in km,  $h_t$  and  $h_r$  are expressed in meters, and  $f$  in MHz. The troposcatter model (3) is used for all ranges exceeding  $r_d$  and calculated for all heights at a given range in parallel with the PE model, which provides the losses from the other propagation mechanisms (standard troposphere, diffraction and reflection). This ensures a uniform approach to all propagation mechanisms of interest in this study. It should be noted that another approach, designed to model turbulence effects from higher altitudes again using PE, was implemented in [50]. The author of [50] added a random fluctuation, obtained by a semi-empirical scatter model, to the mean refractive index profile and applied the PE with the fluctuating profile input. This approach is attractive, but a number of concerns associated with it, which may affect the general application of PE, are also discussed in [50].

It is important to note that, in Equation (3), the aperture-to-medium coupling loss factor is missing, which accounts for the common scattering volume variation with antenna gain, and was added later to the troposcatter loss model [5,28,29]. The respective formulas with a discussion of their use can be found in [5,28,29]. Since the present study uses an omni-directional antenna, the aperture-to-medium coupling loss factor is effectively zero. Contrarily, because the frequency is relatively low and lower antenna heights are used, the original Formula (3) is complemented by the frequency-gain function  $H_0$  as described and derived in [27]. For lower frequencies and antenna heights, the EM energy that reaches the lower part of the common scattering volume (as explained in [27], the most efficient

scattering is in this part) is reduced by reflections from the ground, and this results in  $PL$  increasing, accounted for by  $H_0$ .

### 3. Results and Discussion

In Figures 3–5, the  $M$  profiles used as input to the PE in this study are shown. They were selected from the profiles obtained in [48], where the  $M$  profiles were calculated from meteorological parameters provided by the European Center for Medium-Range Weather Forecasts (ECMWF) for the Bulgarian Black sea shore. The data covers a period of two years. The  $M$  profiles are approximated by linear segments whose number and heights correspond to those for which meteorological parameters were available from ECMWF. Inside the pictures are indicated the exact latitude, longitude, and date to which the profiles refer. In Figures 3 and 4, the profiles named as “first” are at a distance of about 25 km from the shore, and the “second” profiles refer to a distance of about 50 km from the shore to the open sea. Figure 3 presents changes in the profile of a surface-based duct (SBD) when moving from the coast to the open sea; Figure 4 presents the emergence of an elevated duct when moving away from the coast. In Figure 5, the average surface duct profile for summer months at the shore is shown ( $43^\circ$  N– $28^\circ$  E) from the above study as well as a log-linear evaporation duct profile. The resolution of the meteorological data was insufficient to reconstruct the evaporation duct and its profile was not derived from the meteorological data. Instead, it was obtained from Formula (8) for  $z_d = 40$  m [14]:

$$M(z) = M_0 + 0.125 \left[ z - z_d \ln \left( \frac{z + z_0}{z_0} \right) \right], \tag{8}$$

where  $z_0$  is the aerodynamic roughness parameter assumed to be  $1.5 \times 10^{-4}$  m [14,35]. The theory behind Formula (8) defines 40 m as the maximum evaporation duct height;  $z_d$  in Formula (8) determines also the  $M$ -deficit for this duct.

A preliminary estimate of a duct’s ability to capture a specific frequency is made in Formula (9), which provides the maximum wave length,  $\lambda_{max}$ , trapped in a duct [51]:

$$\lambda_{max} = \frac{2}{3} C z_d (\Delta M)^{1/2}, \tag{9}$$

and its relation to the duct thickness  $z_d$  and  $M$ -deficit  $\Delta M$  (see Figure 1). Coefficient  $C$  has different values for the different duct types:  $C = 3.77 \times 10^{-3}$  for surface and surface-based ducts, and  $C = 5.66 \times 10^{-3}$  for elevated ducts. Formula (9) indicates that the AIS frequencies are not trapped by the evaporation duct even though it has the maximal height of 40 m and  $M$ -deficit determined by the most widely used log-linear approximation of its average  $M$  profile, in Equation (8) (see Table 1). Indeed, as it is seen from Table 1, only the second SBD and second elevated duct profiles ensure, according to Equation (9), the full trapping of AIS frequencies. It is important to note that the transition from trapping to non-trapping is gradual and frequencies with  $\lambda$  around  $\lambda_{max}$  can be affected by the duct even though not (entirely) trapped. All subsequent calculations refer to frequency  $F = 161.975$  MHz and horizontal polarization.

In Figures 6 and 7, the  $PL$  curves vs. range for the two SBDs from Figure 3 and the respective troposcatter curves are compared. The troposcatter curves are calculated for values of  $M_0$  corresponding to those of the SBDs. For distances below  $r_d$ , calculated by Formula (7), the troposcatter curves are complemented by the standard troposphere and diffraction  $PL$ . Figures 8 and 9 show analogous results but for the two elevated ducts from Figure 4. The other parameters are:  $h_t = 25$  m and  $h_r = 30$  m for Figures 6 and 8;  $h_t = 55$  m and  $h_r = 30$  m for Figures 7 and 9. The radio horizons are:  $r_{hor} = 43$  km for Figures 6 and 8, and  $r_{hor} = 53$  km for Figures 7 and 9. As expected, the ducting ensures less  $PL$  than troposcattering, even when  $\lambda_{max}$  is less than 1.85 m; this difference in  $PL$  between the two propagation mechanisms starts from a distance of around 30–40 km for Figures 6 and 7, and from a distance of around 100 km for Figures 8 and 9. The beyond-

the-horizon region is characterized by a smooth *PL* increase in the case of SBDs. For the elevated ducts, the beyond-the-horizon region up to a distance of 100 km is characterized by *PL* peaks that exceed (or reach) the troposcattering values (or these of standard troposphere plus diffraction, if the range is less than  $r_d$ ). For the elevated ducts and used  $h_t$ , for lower (receive) antennas, a “skip zone” exits beyond 40 km; see Figure 10 where the *PL* is plotted vs. range and height for  $h_t = 25$  m. In Figure 10, the locations of the two *PL* peaks for the second elevated duct from Figure 8 near a range = 50 km and range = 92 km are clearly visible. In Figure 8, the first peak for the second elevated duct is very well pronounced and increases the *PL* just beyond the horizon with more than 15 dB in comparison to the standard troposphere plus diffraction. The two peaks in Figure 9 are in the diffraction zone. Figures 11 and 12 show *PL* vs. range and height for the second SBD and the first SBD, respectively, and  $h_t = 25$  m. The SBDs are formed with the participation of elevated trapping layers; those layers “pull” the energy upwards and a skip zone is formed close to the Earth surface; see also [11,52]. In comparison to the elevated duct, in the case of SBD, the skip zone does not show *PL* peaks; they are “diffused”, but in the first 30–40 m (for the case of Figure 11), the losses are greater than those above this height. For Figure 12, this zone is lower and its height increases as it approaches 200 km. Looking at Figure 6, one may notice that the weaker first SBD has a lower *PL* than the stronger second SBD. This does not seem unusual, since  $h_r = 30$  m falls within the first 30–40 m of the coverage diagram pattern in Figure 11 but is above the analogous zone with higher losses in Figure 12. In Figure 7, where  $h_t = 55$  m determines a different coverage diagram pattern (not shown here), for the same  $h_r = 30$  m, the situation is as expected: the stronger duct leads to a lower *PL* than the weaker duct. Note also that, in this case, the second SBD is called “stronger” (in comparison to first SBD) because, for it, the AIS frequencies are fully trapped; it is thicker but with a lower M-deficit than the first SBD. This shows the conditional nature of the definition of “stronger” in this case. As it can be seen from the SBD figures, in order to take advantage of ducted propagation, it is not enough to ensure that both the  $h_t$  and  $h_r$  antennas are “immersed” in the duct; their specific heights and location of  $h_r$  in the pattern created by  $h_t$  are very important.

Table 1. Essential duct parameters for the ducts in Figures 3–5.

Type of Duct	$z_d$ , m	$\Delta M$ , M-units	$\lambda_{max}$ , m
SBD 1st profile	175	16	1.76
SBD 2d profile	325	10	2.57
Elevated duct 1st profile	150	2	0.8
Elevated duct 2d profile	325	11.5	4.16
Surface duct	104	12.5	0.92
Evaporation Duct	40	57.44	0.76

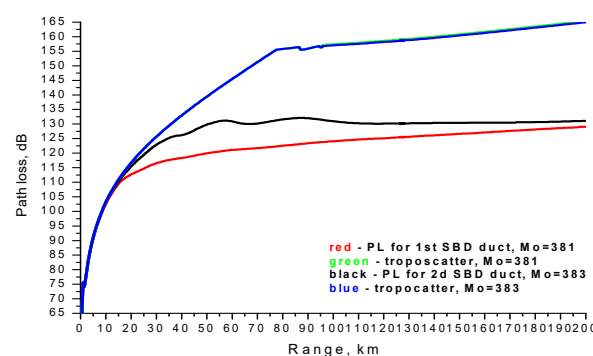


Figure 6. *PL* for SBDs and troposcatter,  $h_t = 25$  m and  $h_r = 30$  m.

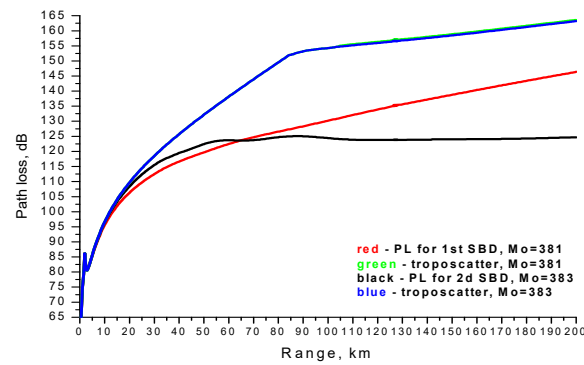


Figure 7. PL for SBDs and troposcatter,  $h_t = 55$  m and  $h_r = 30$  m.

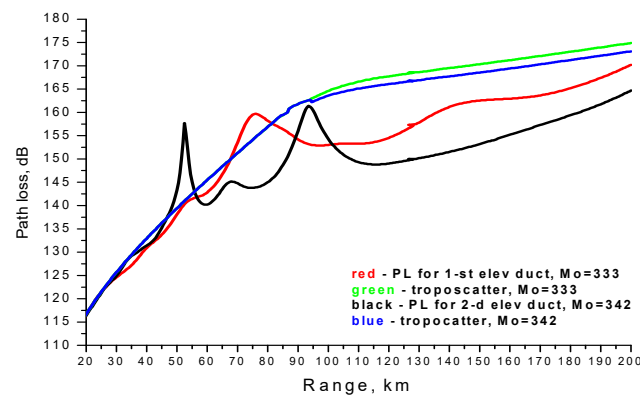


Figure 8. PL for elevated ducts and troposcatter,  $h_t = 25$  m and  $h_r = 30$  m.

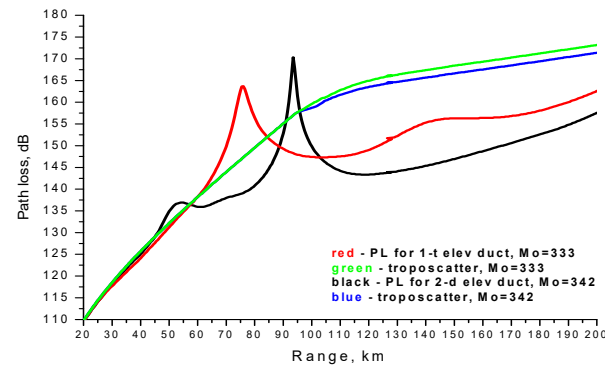


Figure 9. PL for elevated ducts and troposcatter,  $h_t = 55$ ,  $h_r = 30$  m.

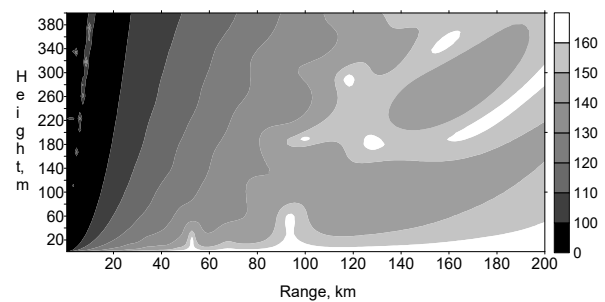


Figure 10. Coverage diagram for the second elevated duct,  $h_t = 25$  m.

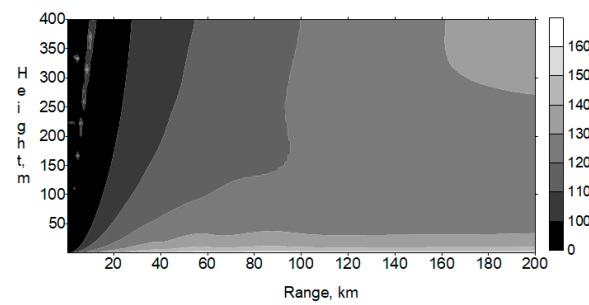


Figure 11. Coverage diagram for the second SBD,  $h_t = 25$  m.

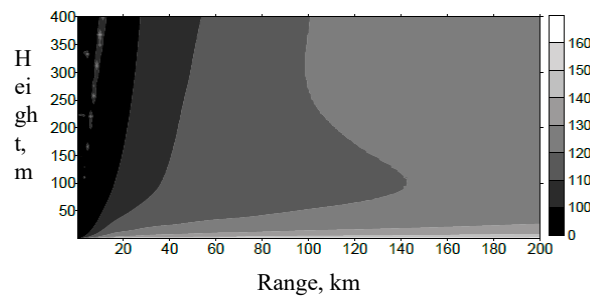


Figure 12. Coverage diagram for the first SBD duct,  $h_t = 25$  m.

Because the elevated ducts are located high above the area of interest for marine propagation, they are often neglected [53]. Indeed, the elevated ducts from Figure 4 result in a higher  $PL$  than the SBDs from Figure 3, but more importantly, the presence of elevated trapping layers forming elevated ducts perturbs the propagation “pattern” in the lower tens of meters above the sea; see Figure 10. Note also that the two ducts from the SBD pair coexisted separated by a distance of 25 km; the same applies to the pair of elevated ducts. Some cases of range-dependent ducting for AIS frequencies are studied in [54]. The present study reports results for only the four characteristic duct types. In Figures 8 and 9, the different values of  $M_0$  lead to a slight difference in troposcatter, whereas in Figures 6 and 7, the two troposcatter curves overlap because the two  $M_0$  values are too close. Note that, according to Formula (3), the higher values of  $M_0$  lead to lower values for troposcatter  $PL$ . The last does not refer to  $PL$  due to ducting. This should be kept in mind when comparing the two propagation mechanisms and the troposcattering is modeled by Formula (3).

In Figure 13, the  $PL$  curves vs. range for the surface duct from Figure 5 for two transmitter heights,  $h_t = 25$  m and  $h_t = 55$  m, and the respective troposcatter curves, calculated by Equation (3), are compared. The receiver height is  $h_r = 30$  m; in this figure, it is seen the influence of the  $h_t$  height on the troposcatter that is rather negligible; see also [5] where the same observation was reported but for a different troposcatter model. Here again, although the AIS frequency is not well trapped, the ducting ensures a significantly lower  $PL$  than the troposcatter. Figure 14 shows  $PL$  vs. the range and height for the surface duct and  $h_t = 25$  m; the  $PL$  increases smoothly with the increase in height and range.

Figure 15 shows the  $PL$  curves for the evaporation duct (with parameters from Table 1), troposcatter and standard troposphere for  $h_t = 55$  m and  $h_r = 30$  m. Compared to the standard troposphere, in the region beyond the horizon, the  $PL$  is reduced by about 10 dB due to the evaporation duct. Note that, after about 140 km, the troposcatter  $PL$  is lower than that of the evaporation duct.

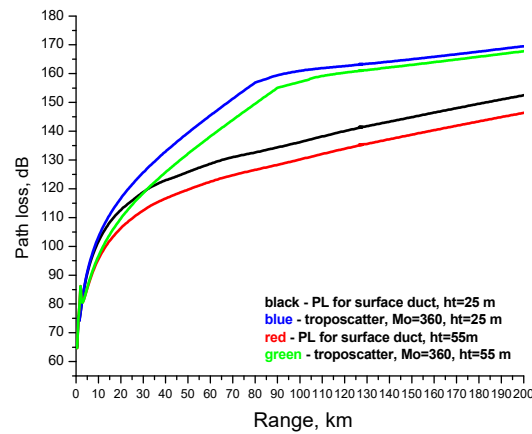


Figure 13. PL for surface duct and troposcatter for  $h_t = 25$  m and  $h_t = 55$  m;  $h_r = 30$  m.

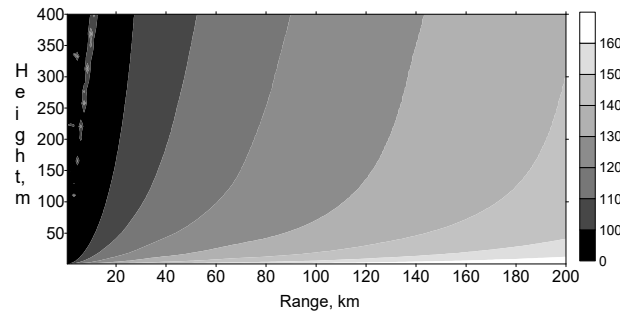


Figure 14. Coverage diagram for the surface duct,  $h_t = 25$  m.

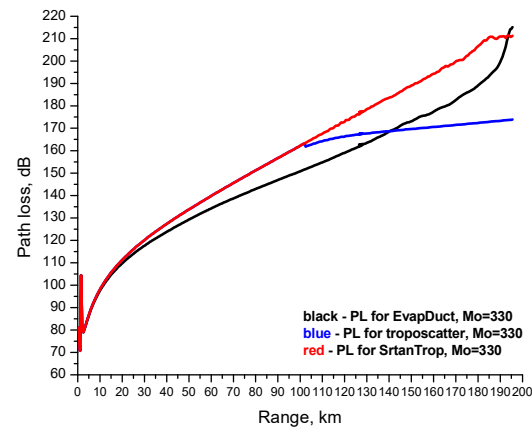


Figure 15. PL for the evaporation duct, standard troposphere and troposcatter,  $h_t = 55$  m and  $h_r = 30$  m.

Figure 16 compares the troposcatter for AIS from [5] for  $h_t = 10$  m and  $h_r = 50$  m, and that calculated by Equation (3) with the same  $h_t$  and  $h_r$ . Two curves were generated by Equation (3): one applies the maximum  $M_0 = 383$  M-units, and the other the minimum  $M_0 = 333$  M-units used in this study. The troposcatter PL calculated by Equation (3) falls between losses not exceeded for 50% of time and those not exceeded for 99% of time. With the increase in the distance, both curves obtained from Equation (3) approach the troposcatter PL from [5], not exceeded for 50% of the time; this is an expected result since the troposcatter model in Equation (3) refers to the median path loss. The difference in PL determined by the two  $M_0$  values can reach 10 dB with the troposcatter model (3).

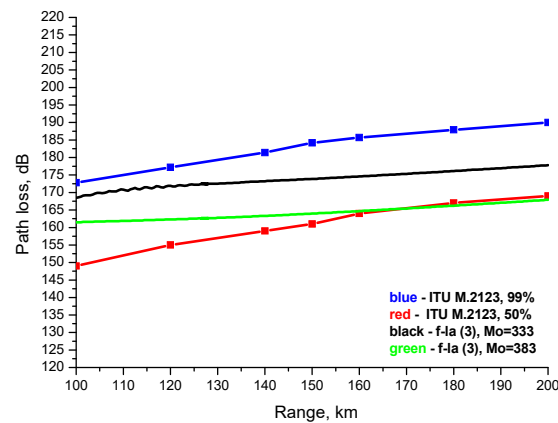


Figure 16. Comparison between the troposcatter model in Equation (3) and [5].

#### 4. Conclusions

This work presented results on the comparison between  $PL$  due to troposphere ducting and  $PL$  due to troposcatter for the AIS frequencies. These two beyond LoS propagation mechanisms were assessed using the PE method, in which a simple troposcatter formula was incorporated. Although a limited set of ducts examples including only the four essential duct types was used, the simulations highlighted some important issues. The simulations showed that the ducting ensures a significantly greater reduction in  $PL$  than troposcatter, and this is valid even when the AIS frequencies are not well trapped in the duct; the evaporation duct is an exception of this “rule”. That is, the most common over-sea duct (and the most studied) is not the best suited to provide deep over-the-horizon propagation for AIS frequencies. Although they are located high above the area of interest, the elevated trapping layers should not be underestimated; it appears that the elevated ducts formed by those layers create a more inhomogeneous propagation environment in the first tens of meters (and beyond) above the sea surface, thus creating the most unfavorable propagation environment as far as ducting is concerned. Special attention should be paid to the skip zones created by elevated trapping layers. In their presence, the coverage pattern created by  $h_t$  is inhomogeneous and sensitive to the height of the  $h_t$ ; depending on the height and location of  $h_r$ , the  $PL$  can be surprisingly high and the ducting propagation mechanism can lose its advantage. In this case, a significant difference between ducting and troposcatter appears: troposcatter is not very sensitive to the height of  $h_t$  and provides smooth  $PL$  curves. Surface and surface-based ducts appear as the main candidates to contribute to the increase in the beyond-the-horizon AIS frequency propagation. These ducts provide a smooth increase in  $PL$  with the increase in range and height; in addition, they are less sensitive to frequency than evaporation ducts, relatively stable in time and extend hundreds of kilometers in space.

This duct–troposcatter comparison can be seen as a preliminary estimate that should be further improved by a more complex troposcatter formulation and the introduction of sea surface roughness for both propagation mechanisms. It should be emphasized that, whatever complex radio wave propagation method is used, it is based on the environmental data that serve as its input. Thus, a good knowledge of the (local and not only) environmental characteristics, such as the availability of irregularities in the troposphere, duct types, their parameters and statistics and the presence of  $M$  profiles with multiple inversions or range dependency (not included in this study), is a prerequisite that will make the inputs to the propagation models more realistic. Only then predicting the propagation beyond the LoS of AIS frequencies with these two anomalous propagation mechanisms can be used for the purpose of increasing the AIS detection range. Additionally, this means that the coastal equipment must be able to evaluate both of these and, possibly, others beyond LoS propagation mechanisms.

**Funding:** This research was funded by the Ministry of Education and Science of Bulgaria (support for ACTRIS BG, part of the Bulgarian National Roadmap for Research Infrastructure).

**Institutional Review Board Statement:** Not applicable.

**Data Availability Statement:** Not applicable.

**Conflicts of Interest:** The author declares no conflict of interest.

## References

1. International Telecommunication Union. *R-REC-M.2092-1: Technical Characteristics for A VHF Data Exchange System in the VHF Maritime Mobile Band*; Electronic Publication: Geneva, Switzerland, 2022.
2. Jiang, S. Networking in ocean: A survey. *ACM Comput. Surv.* **2022**, *54*, 13:1–13:33. [[CrossRef](#)]
3. Wright, D.; Janzen, C.; Bochenek, R.; Austin, J.; Page, E. Marine Observing applications using AIS: Automatic Identification System. *Front. Mar. Sci.* **2019**, *6*, 537. [[CrossRef](#)]
4. Emmens, T.; Amrit, C.; Abdi, A.; Ghosh, M. The promises and perils of Automatic Identification System data. *Expert Sys. Appl.* **2021**, *178*, 114975. [[CrossRef](#)]
5. International Telecommunication Union. *ITU-R M.2123: Long Range Detection of Automatic Identification System (AIS) Messages under Various Tropospheric Propagation Conditions*; ITU: Geneva, Switzerland, 2007.
6. Jo, S.-W.; Shim, W.-S. LTE-Maritime: High-speed maritime wireless communication based on LTE technology. *IEEE Access* **2019**, *7*, 53172–53181. [[CrossRef](#)]
7. Dinc, E.; Akan, O.B. Beyond-line-of-sight communications with ducting layer. *IEEE Commun. Mag.* **2014**, *52*, 37–43. [[CrossRef](#)]
8. Tang, W.; Cha, H.; Wei, M.; Tian, B. Estimation of surface-based duct parameters from automatic identification system using the Levy flight quantum-behaved particle swarm optimization algorithm. *JEWA* **2019**, *33*, 827–837. [[CrossRef](#)]
9. Tang, W.; Cha, H.; Wei, M.; Tian, B.; Li, Y. A Study on the Propagation Characteristics of AIS Signals in the Evaporation Duct Environment. *ACES J.* **2019**, *34*, 996–1001.
10. Robinson, L.; Neue, T.; Burke, J.; Toal, D. A simulated and experimental analysis of evaporation duct effects on microwave communications in the Irish Sea. *IEEE Trans. AP* **2022**, *70*, 4728–4737. [[CrossRef](#)]
11. Shi, Y.; Wang, S.; Yang, F.; Yang, K. Statistical analysis of hybrid atmospheric ducts over the Northern South China sea and their influence on over-the-horizon electromagnetic wave propagation. *J. Mar. Sci. Eng.* **2023**, *11*, 669. [[CrossRef](#)]
12. Bastos, L.; Wietgreffe, H. A Geographical analysis of highly deployable troposcatter systems performance. In Proceedings of the 2013 IEEE Military Communications Conference, San Diego, CA, USA, 18–20 November 2013; pp. 661–667. [[CrossRef](#)]
13. Kerr, D.E. (Ed.) *Propagation of Short Radio Waves*, 2nd ed.; Peter Peregrinus: London, UK, 1987.
14. Paulus, R.A. Practical application of an evaporation duct model. *Radio Sci.* **1985**, *20*, 887–896. [[CrossRef](#)]
15. Yang, C.; Shi, Y.; Wang, J.; Feng, F. Regional spatiotemporal statistical database of evaporation ducts over the South China Sea for future long-range radio application. *IEEE J. Sel. Top. Appl. Earth Obs. Remote Sens.* **2022**, *15*, 6432–6444. [[CrossRef](#)]
16. Yang, N.; Su, D.; Wang, T. Atmospheric ducts and their electromagnetic propagation characteristics in the Northwestern South China Sea. *Remote Sens.* **2023**, *15*, 3317. [[CrossRef](#)]
17. Rautiainen, L.; Tyynelä, J.; Lensu, M.; Siiriä, S.; Vakkari, V.; O'Connor, E.; Hämäläinen, K.; Lonka, H.; Stenbäck, K.; Koistinen, J.; et al. Utö observatory for analysing atmospheric ducting events over Baltic coastal and marine waters. *Remote Sens.* **2023**, *15*, 2989. [[CrossRef](#)]
18. von Engel, A.; Teixeira, J. A ducting climatology derived from ECMWF global analysis fields. *J. Geophys. Res.* **2004**, *109*, D18. [[CrossRef](#)]
19. Yang, C.; Wang, J. The investigation of cooperation diversity for communication exploiting evaporation ducts in the South China Sea. *IEEE Trans. AP* **2022**, *70*, 8337–8347. [[CrossRef](#)]
20. Zaidi, K.S.; Hina, S.; Jawad, M.; Khan, A.N.; Khan, M.U.S.; Pervaiz, H.B.; Nawaz, R. Beyond the horizon, backhaul connectivity for offshore IoT devices. *Energies* **2021**, *14*, 6918. [[CrossRef](#)]
21. Ma, J.; Wang, J.; Yang, C. Long-range microwave links guided by evaporation ducts. *IEEE Commun. Mag.* **2022**, *60*, 68–72. [[CrossRef](#)]
22. Sirkova, I. Anomalous tropospheric propagation: Usage possibilities and limitations in radar and wireless communications systems. In Proceedings of the 10th Jubilee International Conference of the Balkan Physical Union, Sofia, Bulgaria, 26–30 August 2018. [[CrossRef](#)]
23. Valčić, S.; Brčić, D. On detection of anomalous VHF propagation over the Adriatic Sea utilizing a software-defined Automatic Identification System receiver. *J. Mar. Sci. Eng.* **2023**, *11*, 1170. [[CrossRef](#)]
24. Huang, L.-F.; Liu, C.-G.; Wu, Z.-P.; Zhang, L.-J.; Wang, H.-G.; Zhu, Q.-L.; Han, J.; Sun, M.-C. Comparative analysis of intelligent optimization algorithms for atmospheric duct inversion using Automatic Identification System signals. *Remote Sens.* **2023**, *15*, 3577. [[CrossRef](#)]
25. Han, J.; Wu, J.; Zhang, L.; Wang, H.; Zhu, Q.; Zhang, C.; Zhao, H.; Zhang, S. A Classifying-inversion method of offshore atmospheric duct parameters using AIS data based on artificial intelligence. *Remote Sens.* **2022**, *14*, 3197. [[CrossRef](#)]
26. Yeh, L. Simple methods for designing troposcatter circuits. *IRE Trans. Commun. Syst.* **1960**, *8*, 193–198. [[CrossRef](#)]

27. Rice, P.L.; Longley, A.G.; Norton, K.A.; Barsis, A.P. *Transmission Loss Predictions for Tropospheric Communication Circuits*; Department of Commerce, National Bureau of Standards: Gaithersburg, MD, USA, 1965.
28. International Radio Consultative Committee. *Recommendations and Reports of the CCIR: Propagation in Non-Ionized Media*; CCIR: Geneva, Switzerland, 1986.
29. International Telecommunication Union. *Recommendation ITU-R P.452-16: Prediction Procedure for the Evaluation of Interference Between Stations on the Surface of the Earth at Frequencies above about 0.1 Ghz*; Electronic Publication: Geneva, Switzerland, 2015.
30. International Telecommunication Union. *Recommendation ITU-R P.617-2: Propagation Prediction Techniques and Data Required for the Design of Trans-Horizon Radio-Relay Systems*; Electronic Publication: Geneva, Switzerland, 2012.
31. International Telecommunication Union. *Recommendation ITU-R P.2001-3: A General Purpose Wide-Range Terrestrial Propagation Model in the Frequency Range 30 Mhz To 50 Ghz*; Electronic Publication: Geneva, Switzerland, 2019.
32. Li, L.; Wu, Z.-S.; Lin, L.-K.; Zhang, R.; Zhao, Z.-W. Study on the prediction of troposcatter transmission loss. *IEEE Trans. AP* **2016**, *64*, 1071–1079. [[CrossRef](#)]
33. Yuan, D.; Chen, X. Troposcatter transmission loss prediction based on particle swarm optimization. *IET Microw.* **2021**, *15*, 332–341. [[CrossRef](#)]
34. Lee, I.-S.; Noh, J.-H.; Oh, S.-J. A Survey and analysis on a troposcatter propagation model based on ITU-R recommendations. *ICT Express* **2023**, *9*, 507–516. [[CrossRef](#)]
35. Levy, M. *Parabolic Equation Methods for Electromagnetic Wave Propagation*; IEEE: London, UK, 2000.
36. Kuttler, J.R.; Dockery, G.D. Theoretical description of the parabolic approximation Fourier split-step method of representing electromagnetic propagation in the troposphere. *Radio Sci.* **1991**, *26*, 381–393. [[CrossRef](#)]
37. Apaydin, G.; Sevgi, L. *Radio Wave Propagation and Parabolic Equation Modeling*; Wiley-IEEE Press: Hoboken, NJ, USA, 2017.
38. Sirkova, I. Brief review on PE method application to propagation channel modeling in sea environment. *CEJE* **2012**, *2*, 19–38. [[CrossRef](#)]
39. Zhang, P.; Bai, L.; Wu, Z.; Guo, L. Applying the parabolic equation to tropospheric groundwave propagation: A review of recent achievements and significant milestones. *IEEE Antennas Propag. Mag.* **2016**, *58*, 31–44. [[CrossRef](#)]
40. Apaydin, G.; Sevgi, L. The split-step-Fourier and finite-element based parabolic-equation propagation prediction tools: Canonical tests, systematic comparisons, and calibration. *IEEE Antennas Propag. Mag.* **2010**, *52*, 66–79. [[CrossRef](#)]
41. Barrios, A.E.; Anderson, K.; Lindem, G. Low altitude propagation effects—A validation study of the Advanced Propagation Model (APM) for mobile radio applications. *IEEE Trans. AP* **2006**, *54*, 2869–2877. [[CrossRef](#)]
42. Gunashekar, S.D.; Warrington, E.M.; Siddle, D.R.; Valtr, P. Signal strength variations at 2 GHz for three sea paths in the British Channel islands: Detailed discussion and propagation modeling. *Radio Sci.* **2007**, *42*, 1–13. [[CrossRef](#)]
43. Heemskerk, E. RF propagation measurement and model validation during RF/IR synergy trial VAMPIRA. In Proceedings of the SPIE Remote Sensing: Optics in Atmospheric Propagation and Adaptive Systems VIII, Bruges, Belgium, 20–21 September 2005; pp. 598107.1–598107.12. [[CrossRef](#)]
44. Wang, Q.; Alappattu, D.P.; Billingsley, S.; Blomquist, B.; Burkholder, R.J.; Christman, A.J.; Creegan, E.D.; de Paolo, T.; Eleuterio, D.P.; Fernando, H.J.S.; et al. CASPER: Coupled air-sea process and electromagnetic wave ducting research. *Bull. Am. Meteor. Soc.* **2018**, *99*, 1449–1471. [[CrossRef](#)]
45. Wang, J.; Zhou, H.; Li, Y.; Sun, Q.; Wu, Y.; Jin, S.; Quek, T.Q.S.; Xu, C. Wireless channel models for maritime communications. *IEEE Access* **2018**, *6*, 68070–68088. [[CrossRef](#)]
46. Barrios, A.E. Considerations in the development of the advanced propagation model (APM) for U.S. navy applications. In Proceedings of the International Conference on Radar (IEEE Cat. No.03EX695), Adelaide, SA, Australia, 3–5 September 2003; pp. 77–82. [[CrossRef](#)]
47. Wetzell, L.B. *Sea Clutter*; Report 9244; Naval Res. Lab.: Washington, DC, USA, 1990.
48. Sirkova, I. Duct occurrence and characteristics for Bulgarian Black sea shore derived from ECMWF data. *J. Atmos. Sol. Terr. Phys.* **2015**, *135*, 107–117. [[CrossRef](#)]
49. Reed, H.R.; Russell, C.M. *Ultra High Frequency Propagation*; Boston Technical Publishers: Cambridge, MA, USA, 1966.
50. Hitney, H.V. A practical tropospheric scatter model using the parabolic equation. *IEEE Trans. AP* **1993**, *41*, 905–909. [[CrossRef](#)]
51. Turton, J.D.; Bennetts, D.A.; Farmer, S.F.G. An introduction to radio ducting. *Meteorolog. Mag.* **1988**, *117*, 245–254.
52. Rol, M.; Nijboer, R.; Yarovoy, A. Radio wave blind zone in a duct: An analytical approach. In Proceedings of the 24th International Microwave and Radar Conference (MIKON), Gdansk, Poland, 12–14 September 2022; pp. 1–6. [[CrossRef](#)]
53. Couillard, D.; Dahman, G.; GrandMaison, M.-E.; Poitau, G.; Gagnon, F. Robust broadband maritime communications: Theoretical and experimental validation. *Radio Sci.* **2018**, *53*, 749–760. [[CrossRef](#)]
54. Sirkova, I. Automatic Identification System Signals propagation in troposphere ducting conditions. In Proceedings of the 10th IEEE International Black Sea Conference on Communications and Networking (BlackSeaCom), Sofia, Bulgaria, 6–9 June 2022; pp. 331–335. [[CrossRef](#)]

**Disclaimer/Publisher’s Note:** The statements, opinions and data contained in all publications are solely those of the individual author(s) and contributor(s) and not of MDPI and/or the editor(s). MDPI and/or the editor(s) disclaim responsibility for any injury to people or property resulting from any ideas, methods, instructions or products referred to in the content.